electronics

MDPI

Article

Dynamic Fractional-Order Nonsingular Terminal Super-Twisting Sliding Mode Control for a Low-Cost Humanoid Manipulator

Rong Hu [1,2], Xiaolei Xu [1,2], Yi Zhang [1,2,*] and Hua Deng [1,2,*]

[1] School of Mechanical and Electrical Engineering, Central South University, Changsha 410017, China
[2] The State Key Laboratory of High Performance and Complex Manufacturing, Changsha 410083, China
* Correspondence: zhangyicsu@csu.edu.cn (Y.Z.); hdeng@csu.edu.cn (H.D.)

Abstract: Prosthetic humanoid manipulators manufacturing requires light overall weight, small size, compact structure, and low cost to realize wearing purpose. These requirements constrain hardware configuration conditions and aggravate the nonlinearity and coupling effects of manipulators. A dynamic fractional-order nonsingular terminal super-twisting sliding mode (DFONTSM-STA) control is proposed to realize multi-joints coordination for a low-cost humanoid manipulator. This method combines a dynamic fractional-order nonsingular terminal sliding mode (DFONTSM) manifold with the super-twisting reaching law, which can enhance the entire control performance by dynamically changing the position of the sliding mode manifold. By hiding the sign function in a higher-order term, chattering can be effectively suppressed. The stability of the low-cost humanoid manipulator system has been proven based on the Lyapunov stability theory. Experimental results show that the terminal trajectory tracking accuracy of DFONTSM-STA control was promoted by 53.3% and 23.7% respectively compared with FONTSM control and FONTSM-STA control. Thus, the DFONTSM-STA controller is superior in error convergence speed, chattering suppression, and accurate position tracking performance.

Keywords: chattering suppression; fractional-order nonsingular terminal sliding mode controllers; higher-order sliding mode controllers; humanoid manipulator

Citation: Hu, R.; Xu, X.; Zhang, Y.; Deng, H. Dynamic Fractional-Order Nonsingular Terminal Super-Twisting Sliding Mode Control for a Low-Cost Humanoid Manipulator. *Electronics* **2022**, *11*, 3693. https://doi.org/10.3390/electronics11223693

Academic Editor: Jamshed Iqbal

Received: 14 October 2022
Accepted: 8 November 2022
Published: 11 November 2022

1. Introduction

Humanoid manipulators have the characteristics of light weight, small size, strong nonlinearity, coupling, friction, and clearance [1–3]. Among them, friction and clearance are disturbances that significantly influence the control performances of humanoid manipulators. As sliding mode control has the excellent characteristic of efficiently disturbances settlement [4–7], it is widely used for humanoid manipulators' position-tracking control [8–10]. A low-cost humanoid manipulator further constrains its hardware configuration conditions. Complex and high-precision sensors or motors cannot be used when designing a humanoid manipulator because they are generally large in volume. The sensors and motors with small volumes and high precision are generally quite expensive. Teleoperation systems are also not included for cost-saving purposes [11]. All the above features aggravate the nonlinearity, coupling, and complexity of the low-cost humanoid manipulator's dynamics. Benefiting from their variable structure characteristics, sliding mode controllers possess excellent robustness and anti-disturbance ability [12,13]. However, the alternation between the reaching phase and the sliding phase of a sliding mode controller always accompanies by a phenomenon called chattering [14]. The production of the chattering is related to the sliding mode boundary layer thickness [15]. The system states trajectory always has a certain speed when reaching the manifold, and the inertia makes the system states move across the manifold. After that, the controller input generates a reverse signal to pull the system states back to the sliding mode manifold. However, it must take time. This time

difference makes the system states trajectory deviate from the sliding mode manifold for a certain distance and intensifies the thickness of the boundary layer. In this way, the system states trajectory repeatedly passes through the sliding mode manifold, which is reflected in the macroscopic view as a chattering phenomenon [16,17]. Chattering may cause energy consumption and mechanical system damage problems. Therefore, the chattering problem must be first solved when designing sliding mode controllers, especially for a low-cost humanoid manipulator.

The sign function term in a sliding mode reaching law is not only the key to the rapid convergence of sliding functions but also one of the main causes of chattering [18]. Replacement of the sign function with the saturation function is one way to suppress chattering [19]. Hiding the sign function term in a higher-order term is another effective way to eliminate chattering [20–24]. As the system states enter the quasi-sliding mode, the super-twisting sliding mode (STSM) gains the characteristics of the sign function term and ensures that the sliding function and its derivative converge to zero within a limited time [25–27]. The STSM control which belongs to the second-order sliding mode control only requires information on the sliding function [28]. It contains a power rate term that can reduce the time of the system states arriving in quasi-sliding mode and suppress the chattering more effectively compared with the proportional term [29]. Moreno and Osorio used the Lyapunov stability theory to analyze the stability of the super-twisting algorithm (STA) [30]. The proof process has been used in many STSM controllers. Kali et al. proposed an STSM control for manipulators with uncertainties. [31]. Tayebi-Haghighi et al. designed a high-order STSM controller to address multiple control challenges of robots with verification. [20].

Apart from introducing super-twisting algorithms, adding a fractional-order operator to the sliding mode controller is also an effective way to suppress chattering and improve motion control performance [32]. Applying a fractional-order (FO) operator to a sliding mode controller can enhance the flexibility of the controller, and improve its control performances [32–36]. Among all the fractional-order controllers, fractional-order nonsingular terminal sliding mode (FONTSM) controllers are widely used in manipulators to obtain precise position-tracking performance [37–43]. Tran et al. designed an adaptive fuzzy FONTSM control strategy for a two-degree-of-freedom manipulator and used simulation results to illustrate its control performances [40]. Nojavanzadeh et al. proposed an adaptive FONTSM controller to control robots with uncertainty and external interference and used simulation to verify its effectiveness [41]. Su et al. proposed an adaptive FONTSM controller for a cable-driven manipulator with external interferences, which was verified by simulations [42]. Wang et al. formulated an adaptive sliding mode controller that integrates the advantages of PID and FOTNSM manifold [43]. However, most of the FONTSM controllers were verified by simulations. Only a few papers showed the experimental verification of the FONTSM control for manipulators [44–46]. In the previous work of the authors, a dynamic FONTSM controller was proposed for a class of second-order nonlinear systems with simulation verification [47].

To summarize, super-twisting sliding mode control can effectively accelerate the speed of system states reaching the quasi-sliding mode and suppress the chattering. FONTSM control has superiority in motion control accuracy. The fractional-order nonsingular super-twisting sliding mode (FONTSM-STA) control combines the advantages of the FONTSM manifold and the STA, which not only meets the demand for high tracking accuracy but also suppresses the chattering [45]. However, simply combining these two methods has little effect on the joint error converge speed which is a vital factor for humanoid manipulators to mimic arm movements.

Aiming at the above-mentioned problems, a dynamic fractional-order nonsingular terminal super-twisting sliding mode (DFONTSM-STA) control scheme is proposed for a low-cost humanoid manipulator in this study. The main contributions of this paper are summarized as follows:

(1) A DFONTSM-STA controller is formulated for the control of the low-cost humanoid manipulator by combining the dynamic fractional-order nonsingular terminal sliding mode (DFONTSM) manifold with the super-twisting reaching law, which can effectively improve the control accuracy, quickly force the tracking error of each joint to converge and significantly suppress the chattering. The stability and convergence of the low-cost humanoid manipulator control system are proven based on the Lyapunov stability theory.

(2) Experiments illustrate the superiority and feasibility of the proposed DFONTSM-STA control for the low-cost humanoid manipulator. Compared with FONTSM and FONTSM-STA control, the DFONTSM-STA controller has superior control performance. Its terminal position tracking accuracy is increased by 53.3% and 23.7% respectively. Its chattering of joints one to four is decreased by 54.1%, 51.1%, 46.2%, and 55.1% compared with FONTSM control. Its error convergence speed is accelerated significantly. Joints one and two are converged at the beginning, and joints three and four are accelerated by 43.5% and 33.6%, 72.7%, and 54.6% respectively compared with the FONTSM and FONTSM-STA control.

2. Model Description and Problem Analysis

The low-cost humanoid manipulator is limited by cost, size, and weight, which uses hall sensors that generate three pulses in one turn to read the angle position information. The position is detected by sensors whose resolution converted to the joint is 0.3°. Figure 1 shows the three dimensional (3D) model of the low-cost humanoid manipulator and the Denavit-Hartenberg (D-H) coordinate of each joint. Table 1 shows its D-H parameters. Coordinate $x_0y_0z_0$ represents the base coordinate; $x_1y_1z_1$ and $x_2y_2z_2$ represent the coordinate of shoulder joints one and two; $x_3y_3z_3$ and $x_4y_4z_4$ represent the coordinate of elbow joints three and four; $x_ty_tz_t$ represents the terminal coordinate. The dynamic equation of the four degrees-of-freedoms (DOFs) low-cost humanoid manipulator with friction model is described as follows:

$$M(q)\ddot{q} + C(q,\dot{q}) + G(q) + f(q,\dot{q}) = \tau_r \tag{1}$$

$$f(q,\dot{q}) = f_c sign(\dot{q}) + f_v\dot{q} \tag{2}$$

where $q, \dot{q}$, and $\ddot{q}$ ϵ R^4 respectively represent the position, velocity, and acceleration vectors of every joint; $M(q) \in R^{4\times4}$ is the non-singular inertia matrix; $C(q,\dot{q}) \in R^{4\times4}$ is the centrifugal and Coriolis matrix; $G(q) \in R^4$ represents the gravitational vector; $f(q,\dot{q}) \in R^4$ is the vector of the viscous friction torque at joints; $\tau \in R^4$ denotes the torque input vectors; $f_c = diag(f_{c1},\ f_{c2},\ f_{c3},\ f_{c4})$ denotes every joint coulomb friction torque; $f_v = diag(f_{v1},\ f_{v2},\ f_{v3},\ f_{v4})$ denotes every joint viscous friction coefficient.

Table 1. The parameter list of D-H.

Link i	α_{i-1}	a_{i-1}	θ_i	d_i
1	0	0	θ_1 (0°)	0
2	90°	0	θ_2 (−90°)	0
3	90°	0	θ_3 (−90°)	d_3 = −313 mm
4	90°	0	θ_4 (−180°)	0
Terminal	0°	0	θ_5 (0°)	d_5 = −441 mm

The low-cost humanoid manipulator contains four joints to mimic shoulder and elbow movements. To suppress chattering and improve both the error convergence speed and the tracking accuracy, it is necessary to design a new sliding mode control method. As the STSM control hides the sign function in higher order, it possesses a better effect on chattering suppression. Apart from the chattering suppression requirement, the low-cost humanoid manipulator also needs precise trajectory tracking accuracy for mimicking human arm movements. The DFONTSM manifold can enhance the entire control performance by dynamically changing the position of the sliding mode manifold [47]. The steady-state

accuracy can be improved because the fractional-order operator has the characteristics of heredity and memory, which can describe detailed information and increase the flexibility of the control law. Therefore, to solve the trajectory tracking performances of the low-cost humanoid manipulator, this paper proposes a DFONTSM-STA control method that combines a DFONTSM manifold with a super-twisting reaching law.

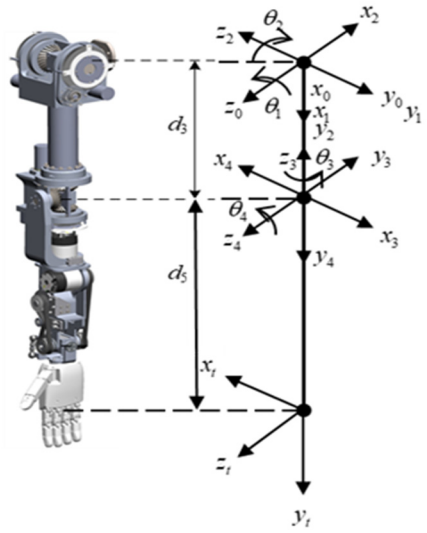

Figure 1. Three dimensional (3D) model and Denavit-Hartenberg (D-H) coordinate of the low-cost humanoid manipulator.

3. DFONTSM-STA Control for the Low-Cost Humanoid Manipulator

This section will briefly present some definitions and lemmas that are needed in the stability proof of the proposed DFONTSM-STA controller.

Definition 1. *The general representation of the FO derivative-integral operator is expressed by Equation (3), [48]*

$$ {}_{t_0}D_t^{\lambda} = \begin{cases} \frac{d^{\lambda}}{dt^{\lambda}} & \lambda > 0 \\ 1 & \lambda = 0 \\ I^{\lambda} = \int_0^t (dt)^{-\lambda} & \lambda < 0 \end{cases} \tag{3} $$

where λ is the FO and t_0 is the initial time. The operator ${}_{t_0}D_t^{\lambda}$ is the symbol for the FO, integral and constant operator.

Definition 2. *The λ th-order Riemann–Liouville (RL) fractional and integral are presented as Equations (4) and (5) [48].*

$$ D^{\lambda} f(t) = \frac{d^{\lambda} f(t)}{dt^{\lambda}} = \frac{1}{\Gamma(m-\lambda)} \bullet \frac{d^m}{dt^m} \bullet \int_{t_0}^{t} \frac{f(\tau)}{(t-\tau)^{\lambda-m+1}} d\tau \tag{4} $$

$$ {}_{t_0}I_t^{\lambda} f(t) = \frac{1}{\Gamma(\alpha)} \bullet \int_{t_0}^{t} \frac{f(t)}{(t-\tau)^{1-\lambda}} d\tau \tag{5} $$

where $m-1 < \lambda < m$, $m \in N$.

Property 1. *[48] if $\alpha \in C$, $\beta \in C$, $\Re e(\alpha) > 0$, $\Re e(\beta) > 0$ and $f(a,b) \in Lp(a,b)$ $(1 \le p \le \infty)$, then $I_{t-}^{\alpha} I_{t-}^{\beta} f(x) = I_{t-}^{\alpha+\beta} f(x)$, $I_{t+}^{\alpha} I_{t+}^{\beta} f(x) = I_{t+}^{\alpha+\beta} f(x)$; $D_{t-}^{\alpha} I_{t-}^{\alpha} f(x) = f(x)$, $D_{t+}^{\alpha} I_{t+}^{\alpha} f(x) = f(x)$.*

Lemma 1. *[44]. Supposing parameters $a_1, a_2, \cdots, a_n$; $0 < p < 2$ are positive, then the following inequality about $a_1, a_2, \cdots, a_n$ and p can be obtained:*

$$\left(a_1^2 + a_2^2 + \cdots + a_n^2\right)^p \leq \left(a_1^p + a_2^p + \cdots + a_n^p\right)^2$$

Lemma 2. *[38,44]. For a Lyapunov function $V(x)$, assuming that V_0 is its initial value and $\alpha \in C$, $\beta \in C$, then*

$$\dot{V}(x) + \alpha V(x) + \beta V^{\gamma}(x) \leq 0, \alpha, \beta > 0, 0 < \gamma < 1 \tag{6}$$

The corresponding settling time can be calculated as

$$T \leq \alpha^{-1}(1-\gamma)^{-1} \ln\left(1 + \alpha\beta^{-1} V_0^{1-\gamma}\right) \tag{7}$$

The FONTSM manifold parameter transforms into the function k^* that calculates the error by exponential function is designed as Equation (9). Then the DFONTSM manifold (8) is formulated for the system described in the model (1) [47].

$$s = \dot{e} + k^* D^{\lambda-1}[sig(e)^{\alpha}] \tag{8}$$

$$k^* = \frac{k_0}{\delta_0 + \rho_0 \cdot \delta_0 \cdot \exp^{-\alpha_\kappa |e|}} \tag{9}$$

where $0 < \lambda_i < 1$, $i = 1 \sim 4$, D^{λ} is the FO operator; $\delta_0 = \mathrm{diag}(\delta_{0i})$ is the diagonal matrix and $\delta_{0i} \in (0,1)$; $\rho_0 = \mathrm{diag}(\rho_{0i})$ and $\alpha_\kappa = \mathrm{diag}(\alpha_{\kappa i})$ are tuning matrices and $\rho_{0i}, \alpha_{\kappa i} \in (0, +\infty)$; $e = \begin{bmatrix} q_{d1} - q_1, & \cdots & q_{d4} - q_4 \end{bmatrix} \in R_4$ denotes the tracking error vector between the target joint rotation angle and the actual joint rotation angle. $k_0 = diag(k_{0i})$ is a positive diagonal matrix. i can be chosen from one to four.

$$sig(e)^{\alpha} = \begin{bmatrix} |e_1|^{\alpha_1} sgn(e_1), & \cdots, & |e_4|^{\alpha_4} sgn(e_4) \end{bmatrix}^T$$

where α is the exponential parameter, which satisfies the relation: $1 > \alpha > 0$. A super-twisting reaching law from [31] is adopted.

$$\begin{aligned} \dot{s} &= -\rho_1 |s|^{1/2} sgn(s) + \omega \\ \dot{\omega} &= -\rho_3 sgn(s) \end{aligned} \tag{10}$$

where $k_1 = \mathrm{diag}(k_{1i})$, $k_2 = \mathrm{diag}(k_{2i})$ are constant matrices and $0 < b = b_1 = \cdots = b_4 < 1$, $i = 1 \sim 4$; With the above reaching law (10), the error vector $(e, \dot{e})$ can be forced to zero. Derivating the DFONTSM manifold (8), we have:

$$\dot{s} = \ddot{e} + k^* \cdot D^{\lambda}[sig(e)^{\alpha}] + \dot{k}^* \cdot D^{\lambda-1}[sig(e)^{\alpha}] \tag{11}$$

where:

$$\dot{k}^* = -\rho_0 \cdot \delta_0 \cdot k_0 \cdot \alpha_\kappa \cdot \dot{e} \cdot \left(\delta_0 + \rho_0 \cdot \delta_0 \cdot \exp^{-\alpha_\kappa \cdot |e|}\right)^{-2} \cdot \exp^{-\alpha_\kappa \cdot |e|} \cdot sign(e) \tag{12}$$

Combining (11) with (10), the control law (14) can be obtained by Equation (13).

$$\ddot{e} + k^* \cdot D^{\lambda}[sig(e)^{\alpha}] + \dot{k}^* \cdot D^{\lambda-1}[sig(e)^{\alpha}] = -\rho_1 |s|^{1/2} sgn(s) + \omega \tag{13}$$

$$\tau_r = M(q)\left(\ddot{q}_d + k^* \cdot D^{\lambda}[sig(e)^{\alpha}] + \dot{k}^* \cdot D^{\lambda-1}[sig(e)^{\alpha}] + \rho_1 |s|^{1/2} sgn(s) + \rho_3 \int_0^t sgn(s) dt\right) + C\left(q, \dot{q}\right) + G(q) \tag{14}$$

4. Stability Proof of DFONTSM-STA Control

The states $\ddot{q}$ can be obtained from the dynamic model (1):

$$\ddot{q} = M(q)^{-1}\left(\tau_r - C\left(q,\dot{q}\right) - G(q) - f\left(q,\dot{q}\right)\right) \tag{15}$$

where $\|f\left(q,\dot{q}\right)\| \leq \|f_{\max}(x,t)\| \leq \overline{F}$. The constant diagonal matrix of $\overline{F}$ represents the friction interference upper boundary. Substituting (14) and (15) into (13), yields:

$$\begin{aligned}\left(\ddot{q}_d - M(q)^{-1}\cdot\left(M(q)\left(\ddot{q}_d + k^*\cdot D^{\lambda}[sig(e)^{\alpha}] + \dot{k}^*\cdot D^{\lambda-1}[sig(e)^{\alpha}] + \rho_1|s|^{1/2}sgn(s) + \int_0^t \rho_3 sgn(s)dt\right) + C\left(q,\dot{q}\right) + G(q)\right.\right.\\ \left.\left. - C\left(q,\dot{q}\right) - G(q) - f\left(q,\dot{q}\right)\right) + k^*\cdot D^{\lambda}[sig(e)^{\alpha}] + \dot{k}^*\cdot D^{\lambda-1}[sig(e)^{\alpha}] = \dot{s}\end{aligned}$$

By simplifying the above equation, error dynamics (16) can be determined:

$$M(q)^{-1}\cdot f\left(q,\dot{q}\right) - \rho_1|s|^{1/2}sgn(s) - \int_0^t \rho_3 sgn(s)dt = \dot{s} \tag{16}$$

Rewrite error dynamics (16) as the form as follows:

$$\begin{aligned}\dot{s} &= -\rho_1|s|^{1/2}sgn(s) + \omega\\ \dot{\omega} &= -\rho_3 sgn(s) + \dot{\varepsilon}\end{aligned} \tag{17}$$

where ε is formulated from (16) and (17) as $\varepsilon = M(q)^{-1}\bullet f\left(q,\dot{q}\right) \leq M(q)^{-1}\bullet\overline{F}$, satisfying the inequality equation $\left|\dot{\varepsilon}\right| \leq \delta_{\varepsilon}$, where $\delta_{\varepsilon} > 0$. For each joint, the error dynamics can be written as:

$$\begin{aligned}\dot{s}_i &= -\rho_{1i}|s_i|^{1/2}sgn(s_i) + \omega_i\\ \dot{\omega}_i &= -\rho_{3i}sgn(s_i) + \dot{\varepsilon}_i\end{aligned} \tag{18}$$

where $\varepsilon_i = M(q_i)^{-1}\cdot f\left(q_i,\dot{q}_i\right)$, and $\dot{\varepsilon}_i$ satisfying $\left|\dot{\varepsilon}_i\right| \leq \delta_{\varepsilon i}$, where $\delta_{\varepsilon i} > 0$. The following Lyapunov function is chosen:

$$V = 2\rho_3|s| + \frac{1}{2}\omega^2 + \frac{1}{2}\left(\rho_1|s|^{1/2}sgn(s) - \omega\right)^2 \tag{19}$$

Then the Lyapunov function V_i of each joint of the low-cost humanoid manipulator can be determined as:

$$V_i = 2\rho_{3i}|s_i| + \frac{1}{2}\omega_i^2 + \frac{1}{2}\left(\rho_{1i}|s_i|^{1/2}sgn(s_i) - \omega_i\right)^2 \tag{20}$$

where i represents joint i, and V_i satisfies $V_i \geq 0$.

Supposing $\eta_i = \begin{bmatrix}|s_i|^{1/2}sgn(s_i) & \omega_i\end{bmatrix}^T$ and $P_i = \begin{bmatrix}2\rho_{3i} + \frac{\rho_{1i}^2}{2} & -\frac{\rho_{1i}}{2}\\ -\frac{\rho_{1i}}{2} & 1\end{bmatrix}$, then (20) can be rewritten as:

$$V_i = \eta_i^T P_i \eta_i \tag{21}$$

V_i satisfies the following inequality equation:

$$\lambda_{\min}\{P_i\}\|\eta_i\|^2 \leq V_i \leq \lambda_{\max}\{P_i\}\|\eta_i\|^2 \tag{22}$$

where $\lambda_{\min}\{P_i\}$ denotes minimum eigenvalues of P_i and $\lambda_{\max}\{P_i\}$ denotes the maximum eigenvalue. $\|\eta_i\|$ is the Euclidean norm. By rearranging Equation (22), we obtain:

$$\frac{V_i^{\frac{1}{2}}}{\lambda_{\max}^{\frac{1}{2}}\{P_i\}} \leq \|\eta_i\| \leq \frac{V_i^{\frac{1}{2}}}{\lambda_{\min}^{\frac{1}{2}}\{P_i\}} \tag{23}$$

Derivating the Lyapunov function, $\dot{V}_i$ can be expressed as:

$$\dot{V}_i = 2\rho_{3i}\dot{s}_i sgn(s_i) + \omega_i\dot{\omega}_i + \left(\rho_{1i}|s_i|^{1/2}sgn(s_i) - \omega_i\right)\left(\frac{\rho_{1i}}{2}|s_i|^{-1/2}\dot{s}_i - \dot{\omega}_i\right)$$

Substituting error dynamics (18) into the above equation, yields:

$$\begin{aligned}\dot{V}_i &= -2\rho_{1i}\rho_{3i}|s_i|^{1/2} + 2\rho_{3i}\omega_i sgn(s_i) - \rho_{3i}\omega_i sgn(s_i) + \omega_i\dot{\varepsilon}_i + \left(\rho_{1i}|s_i|^{1/2}sgn(s_i) - \omega_i\right) \\ &\quad \cdot\left(\tfrac{\rho_{1i}}{2}|s_i|^{-1/2}\left(-\rho_{1i}|s_i|^{1/2}sgn(s_i) + \omega_i\right) - \left(-\rho_{3i}sgn(s_i) + \dot{\varepsilon}_i\right)\right) \\ \dot{V}_i &= \tfrac{1}{|s_i|^{1/2}}\left(-\tfrac{1}{2}\rho_{1i}^3|s_i| + \rho_{1i}^2|s_i|^{1/2}sgn(s_i) - \tfrac{\rho_{1i}}{2}\omega_i^2 - \rho_{1i}\rho_{3i}|s_i|\right) + \dot{\varepsilon}_i\left(-\rho_{1i}|s_i|^{1/2}sgn(s_i) + 2\omega_i\right)\end{aligned}$$

Simplify the above equation into matrix multiple forms:

$$\begin{aligned}\dot{V}_i = -\tfrac{1}{|s_i|^{1/2}}&\begin{bmatrix} |s_i|^{1/2}sgn(s_i) & \omega_i \end{bmatrix}\begin{bmatrix} \frac{1}{2}\rho_{1i}^3 + \rho_{1i}\rho_{3i} & -\frac{\rho_{1i}^2}{2} \\ -\frac{\rho_{1i}^2}{2} & \frac{\rho_{1i}}{2} \end{bmatrix}\begin{bmatrix} |s_i|^{1/2}sgn(s_i) \\ \omega_i \end{bmatrix} \\ &+\dot{\varepsilon}_i\begin{bmatrix} -\rho_{1i} & 2 \end{bmatrix}\begin{bmatrix} |s_i|^{1/2}sgn(s_i) \\ \omega_i \end{bmatrix}\end{aligned} \tag{24}$$

Supposing: $A_i = \begin{bmatrix} \frac{1}{2}\rho_{1i}^3 + \rho_{1i}\rho_{3i} & -\frac{\rho_{1i}^2}{2} \\ -\frac{\rho_{1i}^2}{2} & \frac{\rho_{1i}}{2} \end{bmatrix}$, $B_i = \begin{bmatrix} 0 \\ 1 \end{bmatrix}$, $C_i = \begin{bmatrix} 1 \\ 0 \end{bmatrix}$, then Equation (24) can be rewritten as:

$$\dot{V}_i = -\frac{1}{|s_i|^{1/2}}\eta_i^T A_i\eta_i + \frac{2\dot{\varepsilon}_i}{|s_i|^{1/2}}|s_i|^{1/2}B_i^T P_i\eta_i \tag{25}$$

If $\|\dot{\varepsilon}\| \le \|\delta\|$, $|\dot{\varepsilon}_i| \le \delta_i$, then $2\dot{\varepsilon}_i|s_i|^{1/2}B_i^T P_i\eta_i$ satisfies:

$$\begin{aligned}2\dot{\varepsilon}_i|s_i|^{1/2}B_i^T P_i\eta_i &\le \dot{\varepsilon}_i^2|s_i| + \eta_i^T P_i B_i B_i^T P_i^T\eta_i \\ &\le \delta_{\varepsilon i}^2\eta_i^T C_i C_i^T\eta_i + \eta_i^T P_i B_i B_i^T P_i^T\eta_i\end{aligned} \tag{26}$$

By substituting inequality (26) into rearranged $\dot{V}_i$ (25), we obtain the following inequality (27):

$$\dot{V}_i \le -\frac{1}{|s_i|^{1/2}}\eta_i^T\left(A_i - \delta_{\varepsilon i}^2 C_i C_i^T - P_i B_i B_i^T P_i^T\right)\eta_i = -\frac{1}{|s_i|^{1/2}}\eta_i^T Q_i\eta_i \tag{27}$$

where:

$$Q_i = \begin{bmatrix} \frac{1}{2}\rho_{1i}^3 + \rho_{1i}\rho_{3i} - \delta_{\varepsilon i}^2 - \frac{\rho_{1i}^2}{4} & -\frac{\rho_{1i}^2}{2} + \frac{\rho_{1i}}{2} \\ -\frac{\rho_{1i}^2}{2} + \frac{\rho_{1i}}{2} & \frac{\rho_{1i}}{2} - 1 \end{bmatrix} \tag{28}$$

If ρ_{1i} and ρ_{3i} satisfy the following conditions:

$$\begin{aligned}\rho_{1i} &> 2 \\ \rho_{3i} &> \tfrac{\rho_{1i}^3 + 4\delta_{\varepsilon i}^2(\rho_{1i} - 2)}{4\left(\rho_{1i}^2 - 2\rho_{1i}\right)}\end{aligned}$$

then the error dynamics for each joint (18) meet the demands of the Lyapunov stability and the matrix Q_i is symmetrical and positive. Obviously $|s_i|^{1/2} \le \|\eta_i\|$, substituting Equation (23) into Equation (27), $\dot{V}_i$ satisfies:

$$\dot{V}_i \le -\frac{1}{\|\eta_i\|}\lambda_{\min}\{Q_i\}\|\eta_i\|^2 \le -\frac{\lambda_{\min}\{Q_i\}}{\lambda_{\max}^{\frac{1}{2}}\{P_i\}}V_i^{\frac{1}{2}}$$

where term $\lambda_{\min}\{Q_i\}$ denotes the minimum eigenvalues of the matrix Q, $\lambda_{\max}\{Q_i\}$ denotes the maximum eigenvalues. Thus, the converge time T_{ci} for each joint of the low-cost

humanoid manipulator satisfies the following inequality which can be obtained through Lemmas 1 and 2:

$$T_{ci} \leq 2\lambda_{\max}^{1/2}\{P_i\}\lambda_{\min}^{-1}\{Q_i\}V_i^{1/2}(0)$$

Therefore, the control law (14) can ensure the error dynamics of the low-cost humanoid manipulator to be stable.

5. Simulation and Discussion

To reveal the superior performances of the proposed DFONTSM-STA control, we perform simulation verification on the low-cost humanoid manipulator. The coulomb and viscous friction parameters are selected as $f_{c1} = f_{c2} = f_{c4} = 1.25N$, $f_{c3} = 0.125N$, $f_{v1} = f_{v2} = f_{v4} = 1$, $f_{v3} = 0.1$ [44]. The model information of the low-cost humanoid manipulator is listed in Tables 2–4.

Table 2. The center mass position of the connecting rod.

Center Mass Position (m)	Joint One	Joint Two	Joint Three	Joint Four
X	0	-0.04×10^{-3}	0	-0.94×10^{-3}
Y	0	125.16×10^{-3}	-7×10^{-3}	166.42×10^{-3}
Z	11.57×10^{-3}	7.71×10^{-3}	-0.26×10^{-3}	6.97×10^{-3}

Table 3. Mass of connecting rod of the humanoid manipulator.

Mass (kg)	Rod One	Rod Two	Rod Three	Rod Four
M	728.22×10^{-3}	7016.49×10^{-3}	382.18×10^{-3}	3341.64×10^{-3}

Table 4. Connecting rod inertia of humanoid manipulator.

Moment of Inertia ($\mathbf{kg \cdot m^2}$)	Rod One	Rod Two	Rod Three	Rod Four
Ixx	$1{,}709{,}909.71 \times 10^{-9}$	$26{,}245{,}6649.98 \times 10^{-9}$	$625{,}787.92 \times 10^{-9}$	$158{,}795{,}139.03 \times 10^{-9}$
Iyy	$875{,}916.10 \times 10^{-9}$	$20{,}863{,}623.56 \times 10^{-9}$	$544{,}829.79 \times 10^{-9}$	$2{,}996{,}242.06 \times 10^{-9}$
Izz	$1{,}375{,}449.61 \times 10^{-9}$	$249{,}837{,}989.90 \times 10^{-9}$	$270{,}182.90 \times 10^{-9}$	$157{,}591{,}605.74 \times 10^{-9}$
Ixy	24.45×10^{-9}	$-46{,}664.65 \times 10^{-9}$	13.85×10^{-9}	$-1{,}391{,}395.68 \times 10^{-9}$
Iyz	-47.57×10^{-9}	$17{,}384{,}004.90 \times 10^{-9}$	279.02×10^{-9}	$707{,}363.35 \times 10^{-9}$
Ixz	16.53×10^{-9}	$185{,}311.42 \times 10^{-9}$	-2.14×10^{-9}	$107{,}519.45 \times 10^{-9}$

5.1. Comparison of Simulation Results

To better compare and analyze the performances of the FONTSM control (29) [44], FONTSM-STA control (30) [45], and DFONTSM-STA control (14), we select control parameters listed in Tables 5 and 6. The simulation performances are described in Figures 2–6.

$$\tau_r = M(q)\left(\ddot{q}_d + k \cdot D^{\lambda}[sig(e)^{\alpha}] + k_2 sig(s)^b + k_1 s\right) + C(q,\dot{q}) + G(q) \quad (29)$$

$$\tau_r = M(q)\left(\ddot{q}_d + k \cdot D^{\lambda}[sig(e)^{\alpha}] + \rho_1 |s|^{1/2} sgn(s) + \rho_3 \int_0^t sgn(s)dt\right) + C(q,\dot{q}) + G(q) \quad (30)$$

Table 5. Parameters list of dynamic fractional-order nonsingular terminal super-twisting sliding mode (DFONTSM-STA) control.

	ρ_1	ρ_2	α_κ	δ_0	k_0	α	λ	ρ_0
Joint one	40	4	1	0.1	2	0.8	0.9	2
Joint two	40	4	1	0.1	2	0.8	0.9	2
Joint three	70	4	1	0.1	2	0.8	0.9	0.8
Joint four	70	4	1	0.1	2	0.8	0.9	0.8

Table 6. Parameters list of fractional-order nonsingular terminal super-twisting sliding mode (FONTSM-STA) control and fractional-order nonsingular terminal sliding mode (FONTSM) control.

	k_1	ρ_1	k_2	ρ_2	k_0	α	λ
Joint one	60	40	6	4	1	0.8	0.9
Joint two	60	40	6	4	1	0.8	0.9
Joint three	80	70	6	4	4	0.8	0.9
Joint four	80	70	6	4	4	0.8	0.9

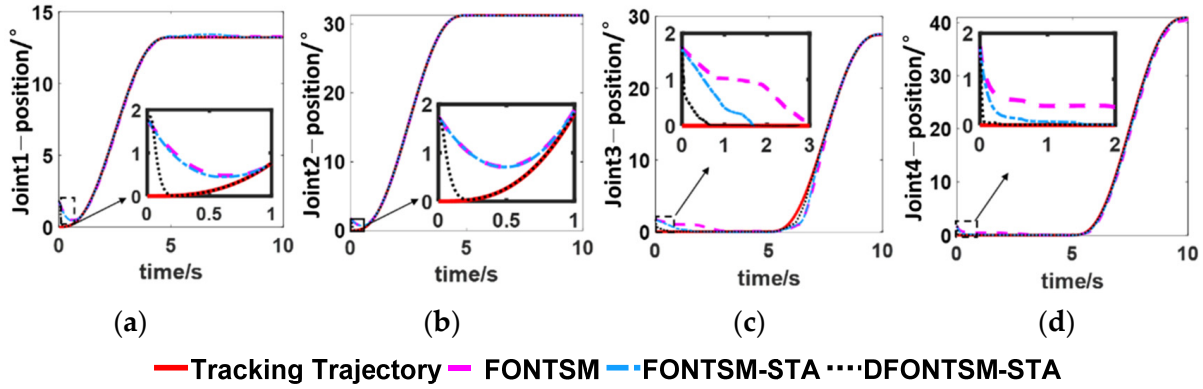

Figure 2. Position tracking trajectory of each joint. (**a**): joint one; (**b**): joint two; (**c**): joint three; (**d**): joint four.

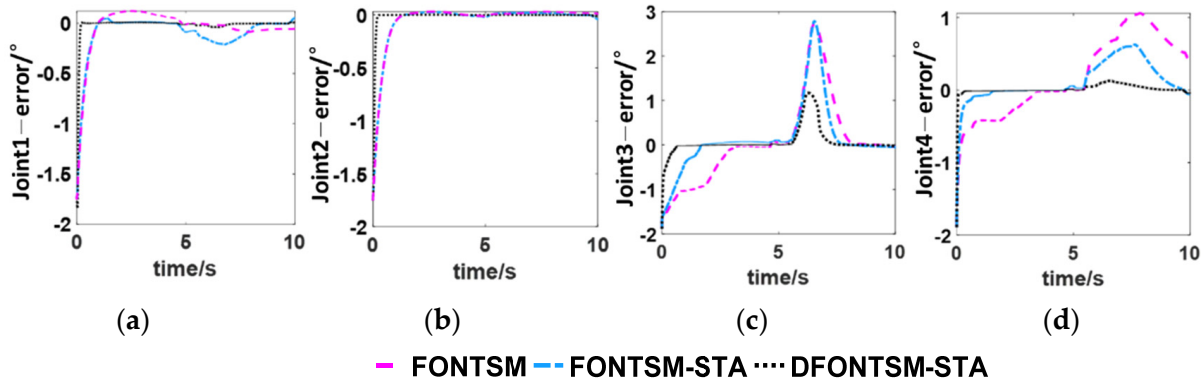

Figure 3. The position tracking error of each joint. (**a**): joint one; (**b**): joint two; (**c**): joint three; (**d**): joint four.

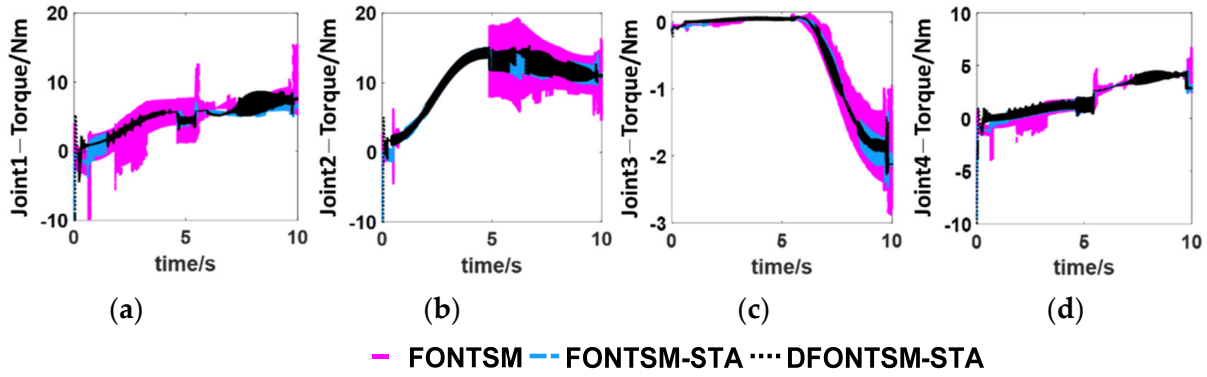

Figure 4. Control input torque of each joint (**a**): joint one; (**b**): joint two; (**c**): joint three; (**d**): joint four.

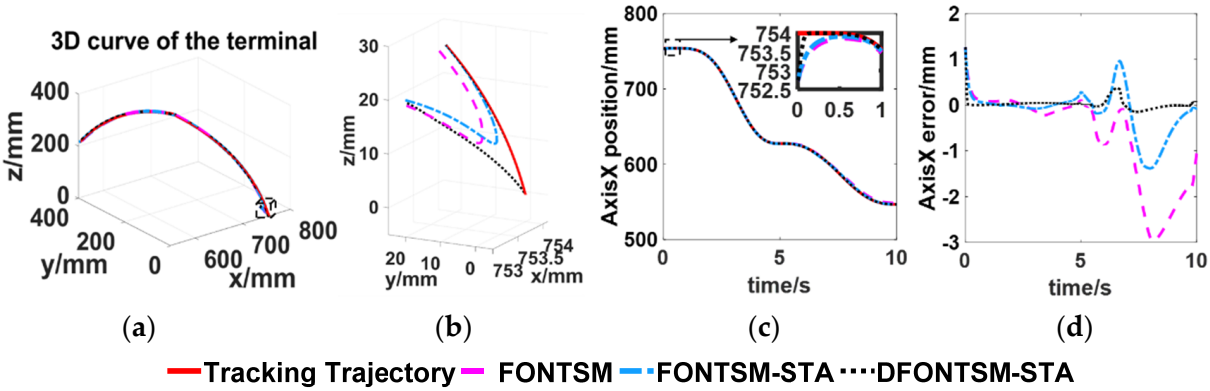

Figure 5. Terminal motion trajectory and its tracking error (**a**): Terminal trajectory tracking curve under base coordinate; (**b**): Terminal trajectory tracking error; (**c**): axis X position; (**d**): axis X error.

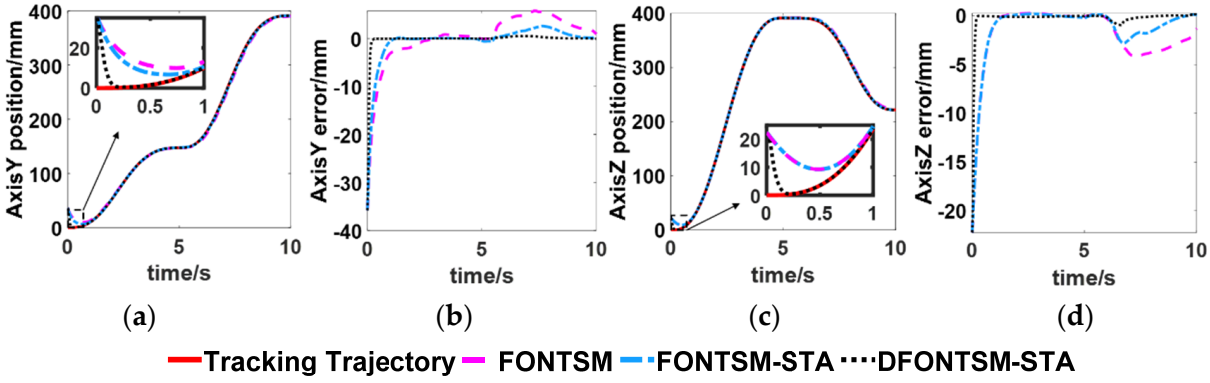

Figure 6. Terminal motion trajectory and its tracking error on Y axis and Z axis of the base coordination. (**a**): axis Y position; (**b**): axis Y error; (**c**): axis Z position; (**d**): axis Z error.

5.2. Simulation Analysis

The convergence time is calculated when the tracking error accuracy is within 0.5° (shoulder joints) or 1° (elbow joints), which is shown in Table 7. Table 8 shows the maximum amplitude of control torque variations in a small time interval of each joint. The variations of torque in a small interval reflect the degree of chattering suppression, we defined an indicator shown as equation (31) to facilitate analysis and to directly evaluate the controller's chattering suppression performance.

$$|\tau|_{\max} = \left|\tau(t) - \tau\left(t - t_p\right)\right| \tag{31}$$

where t_p is the time interval between the two calculated torques and t_p = 20 ms is defined in this simulation.

Table 7. Convergence time for each joint.

$\|e\| \leq 0.5°$ $\|e\| \leq 1°$	DFONTSM-STA (t_{conv})s	FONTSM-STA (t_{conv})s	FONTSM (t_{conv})s
Joint one	0.101	0.409	0.443
Joint two	0.090	0.464	0.464
Joint three	0.036	0.515	1.309
Joint four	0.021	0.067	0.098

Table 8. The maximum amplitude of the low-cost humanoid manipulator control torque variations.

$\|\tau\|_{max}$ t_p = 20 ms	DONTSM-STA	FONTSM-STA	FONTSM
Joint one	4.2875	3.7355	12.7760
Joint two	3.5760	4.3541	7.4774
Joint three	0.7294	0.6397	0.9683
Joint four	2.0093	2.1479	4.2029

As shown in Table 7, the tracking error convergence speed of the DFONTSM-STA control is faster than that of FONTSM and FONTSM-STA control. Compared with FONTSM control, the error convergence time by DFONTSM-STA control from joints one to four is reduced by 77.2%, 80.6%, 97.2%, and 78.6% respectively. Compared with the FONTSM-STA control, the convergence time is reduced by 75.3%, 80.6%, 93.0%, and 68.7% respectively. It can be concluded that under the control of DFONTSM-STA, each joint of the low-cost humanoid manipulator takes the least time to converge.

The DFONTSM-STA control and the FONTSM-STA control also have better chattering suppression effects compared with the FONTSM control. When t_p = 20 ms, the maximum chattering variations of joints one to four under FONTSM-STA control are reduced by 70.8%, 41.8%, 33.9%, and 48.9% compared with the FONTSM control. While under DFONTSM-STA control, the maximum chattering variations for joints one to four are reduced by 66.4%, 52.1%, 24.7%, and 52.2% compared with the FONTSM control. From Figure 4, it can be seen that the control inputs under the FONTSM control have the most severe high-frequency chattering among the three control methods. If the unmodeled dynamics of the low-cost humanoid manipulator are excited by high-frequency chattering, the moving trajectory may diverge, which will destroy the machine structure and cause security compromises.

Compared with the FONTSM-STA and FONTSM methods, DFONTSM-STA adds dynamic characteristics to the sliding manifold, which can make the sliding manifold change dynamically according to the actual error. Therefore, among these three methods, the DFONTSM-STA controller has the strongest ability to maintain the error at zero, and the best joint error convergence performance.

From Table 9, the data of terminal position root mean square error indicates that compared with the FONTSM control, the terminal root mean square tracking error (S_{rmste}) under DFONTSM-STA control are decreased by 90.9%, 57.4%, and 57.1% in the x-direction, y-direction, and z-direction of the low-cost humanoid manipulator. Furthermore, under DFONTSM-STA control, the S_{rmste} in X, Y, and Z directions are further reduced by 78.2%, 43.7%, and 51.3% with the comparison of the FONTSM-STA control. The S_{rmste} of the distance between the terminal and the target under DFONTSM-STA control is limited within 3 mm and decreased by 46.7% and 58.0% with the comparison of FONTSM-STA and FONTSM control respectively. Thus, adding dynamic characteristics can not only improve the joint error convergence but also greatly improve the terminal error convergence.

Table 9. Terminal position root mean square error.

S_{rmste} (mm)	DFONTSM-STA	FONTSM-STA	FONTSM
Axis x	0.1126	0.5165	1.2403
Axis y	2.3329	4.1434	5.4771
Axis z	1.5838	3.2514	3.6918
Distance between terminal and target	2.8220	5.2921	6.7206

To sum up, the DFONTSM-STA control has the biggest possibility to realize the terminal trajectory tracking with smooth and accurate movements.

6. Experimental Verification

6.1. Experiment Setting

Figure 7 displays the experimental platform. The core components of the low-cost humanoid manipulator system are as follows: the PC; the hardware controller; EPOS4 drivers; Maxon DC motors. The PC calculates each joint's control input. The hardware controller has data transmission functions. It uses EtherCAT as the communication channel to exchange position and torque data with the PC; EPOS4 drivers support the CANopen protocol. Its communication speed can reach to 1 Mbps. The hall sensor whose resolution converted to joints is 0.3° for obtaining angular position information was inserted in the Maxon DC motor. By debugging the above hardware, a real-time system has been constructed to control the low-cost humanoid manipulator. The parameters of the three controllers in experiments are listed in Tables 10 and 11.

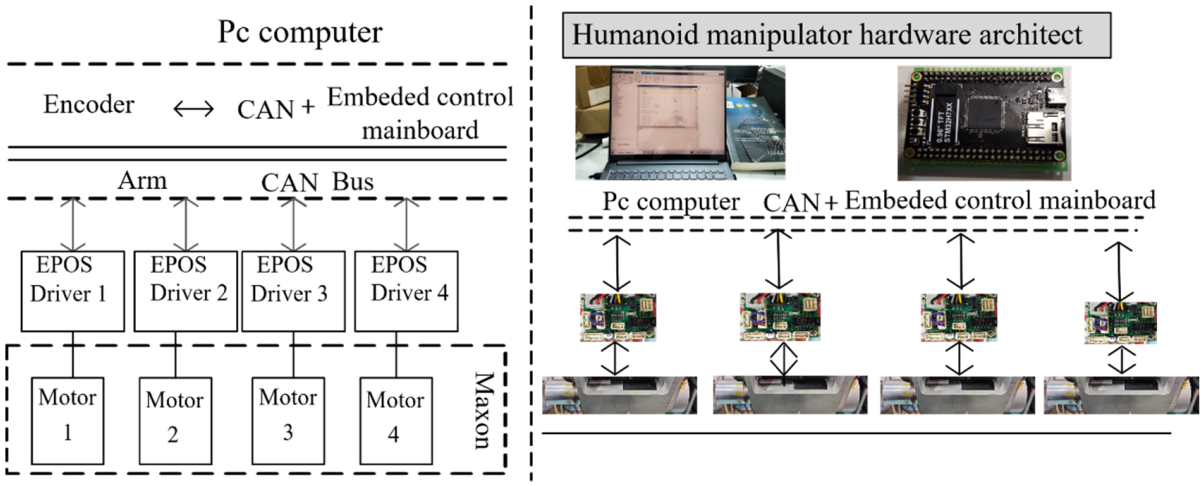

Figure 7. The architecture of the humanoid manipulator system.

Table 10. Parameters of DFONTSM-STA control.

	ρ_1	ρ_2	α_κ	δ_0	k_0	α	λ	ρ_0
Joint one	6	6	1	0.05	1	0.8	0.9	1
Joint two	6	6	1	0.05	1	0.8	0.9	1
Joint three	3	3	1	0.05	1	0.8	0.9	2
Joint four	3	3	1	0.05	1	0.8	0.9	2

Table 11. Parameters of FONTSM-STA and FONTSM control.

	k_1	ρ_1	k_2	ρ_2	k_0	α	λ
Joint one	9.5	6	6	6	15	0.8	0.9
Joint two	9.5	6	6	6	15	0.8	0.9
Joint three	6.5	3	3	3	15	0.8	0.9
Joint four	6.5	3	3	3	15	0.8	0.9

The experiments adapt the trajectories in the simulation as the target of the low-cost humanoid manipulator. The control performances of DFONTSM-STA control, FONTSM-STA control, and FONTSM control are compared. The simulation movements and physical schematic of the low-cost humanoid manipulator are shown in Figure 8.

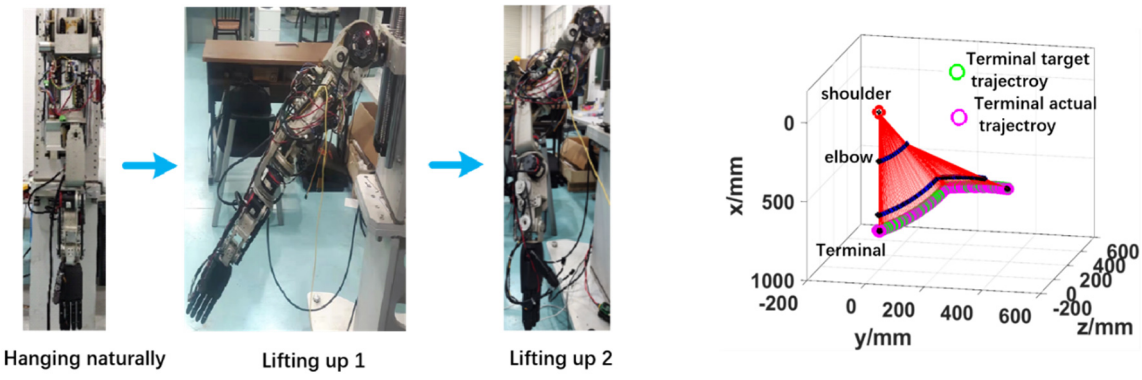

(**a**) (**b**)

Figure 8. Simulation and physical schematic of humanoid manipulator movement. (**a**): Physical schematic (**b**): The simulation movement.

6.2. Experiment Results

Figures 9–18 present the experimental performances of the low-cost humanoid manipulator.

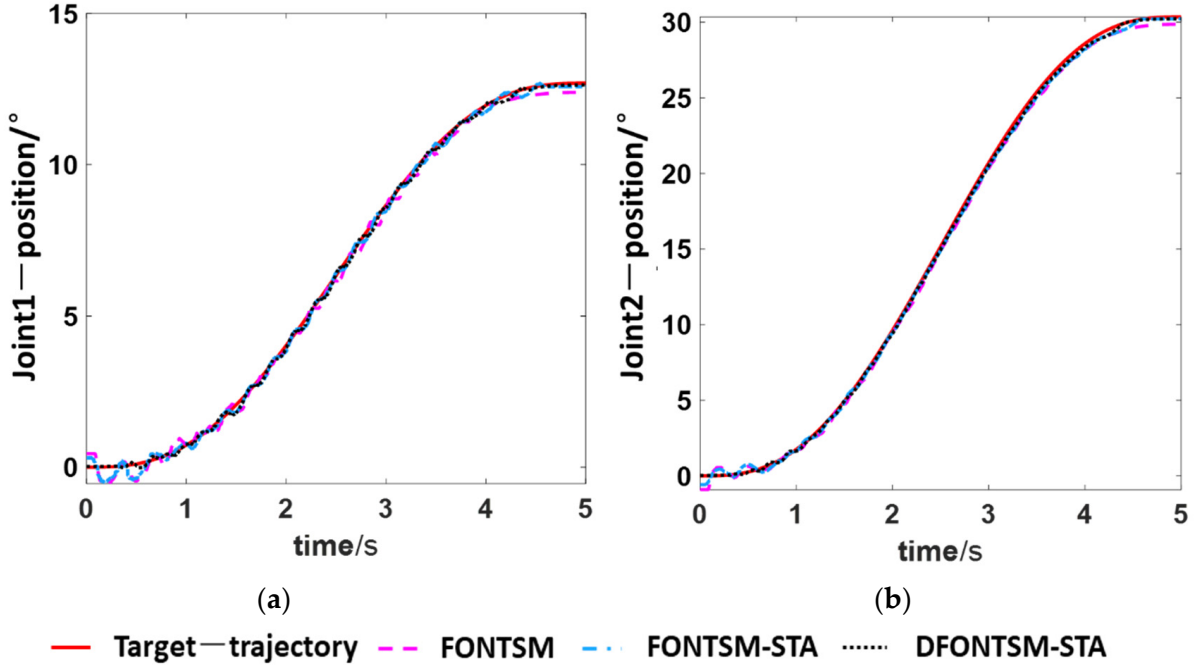

(**a**) (**b**)

Figure 9. Position tracking trajectories of the shoulder joints. (**a**): joint one; (**b**): joint two.

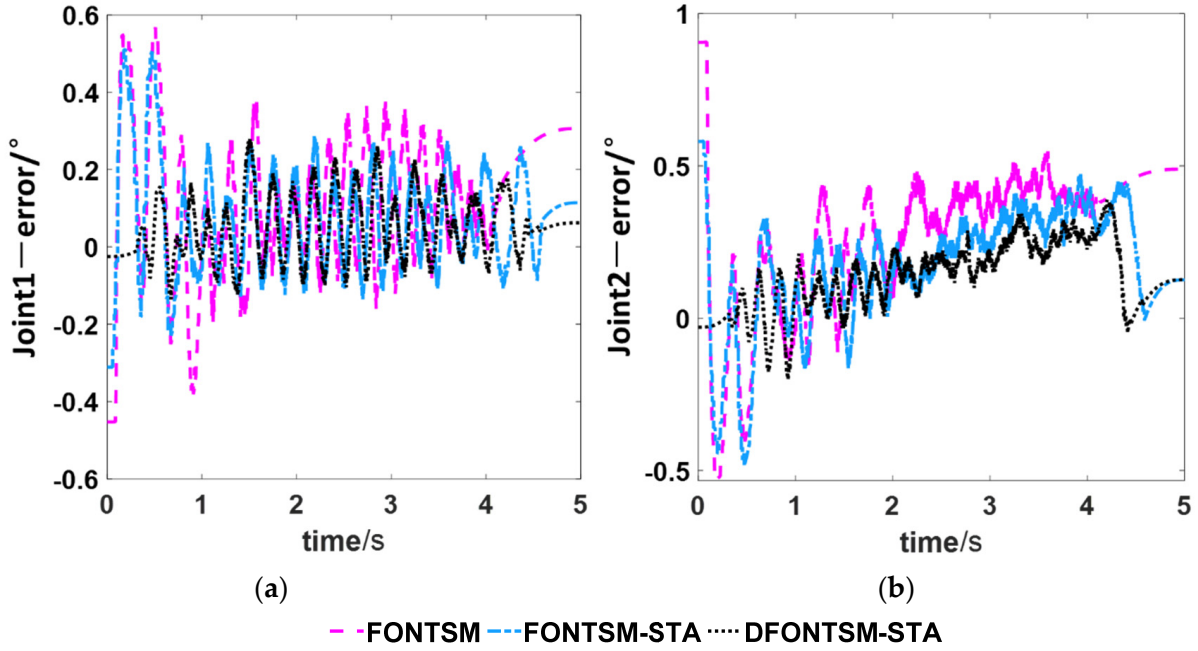

Figure 10. Position tracking errors of the shoulder joints. (**a**): joint one; (**b**): joint two.

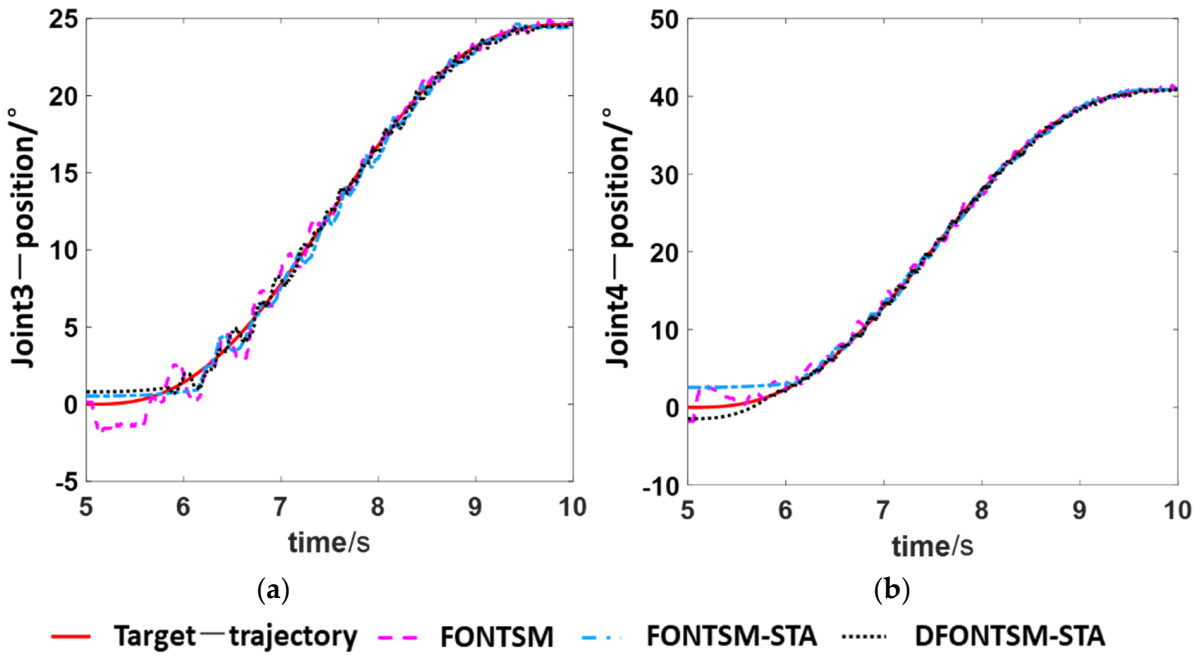

Figure 11. Position tracking trajectories of the elbow joints. (**a**): joint three; (**b**): joint four.

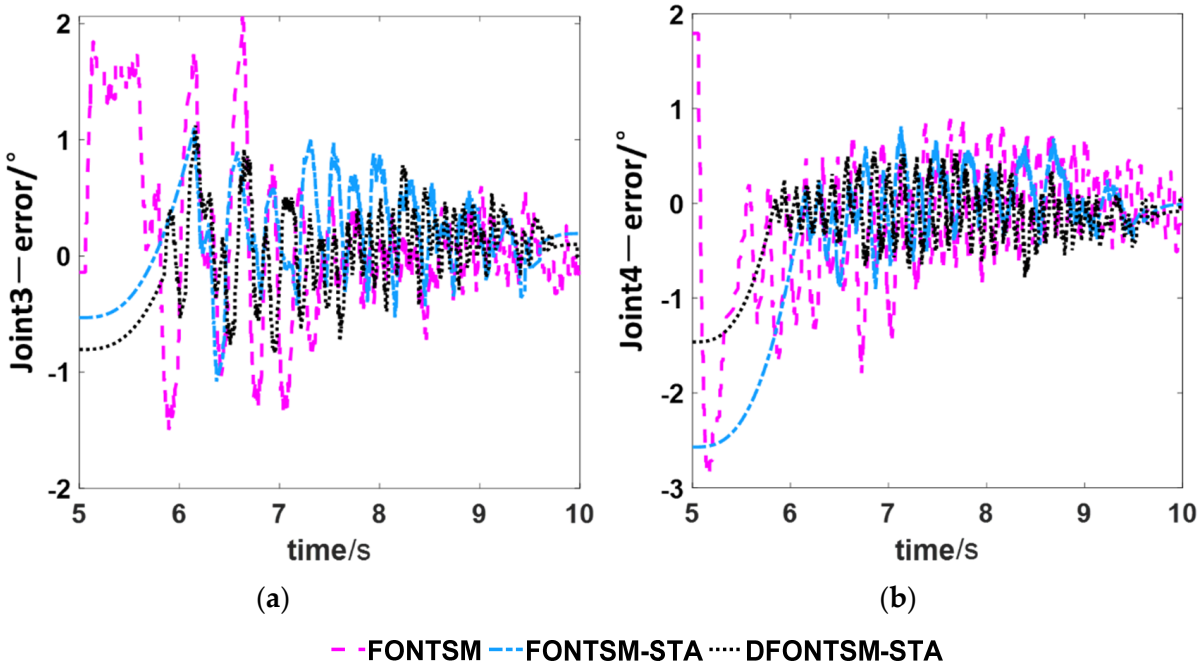

Figure 12. The position tracking error of the elbow joints. (**a**): joint three; (**b**): joint four.

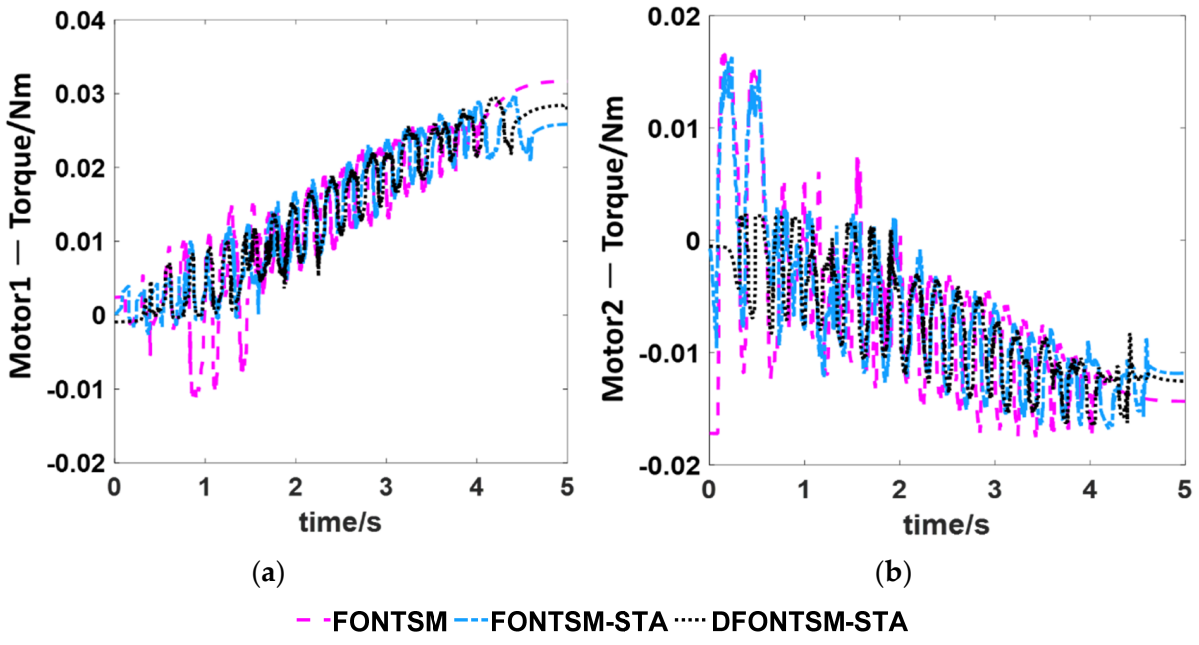

Figure 13. Input torques of the shoulder joints. (**a**): joint one; (**b**): joint two.

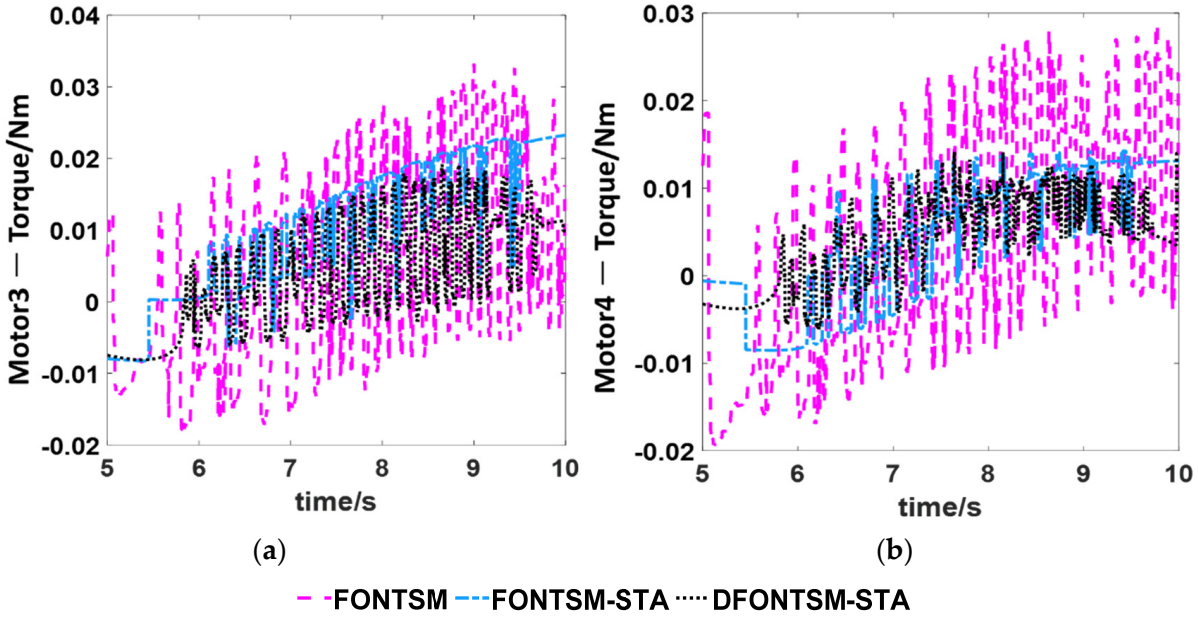

Figure 14. Input torques of elbow joints. (**a**): joint three; (**b**): joint four.

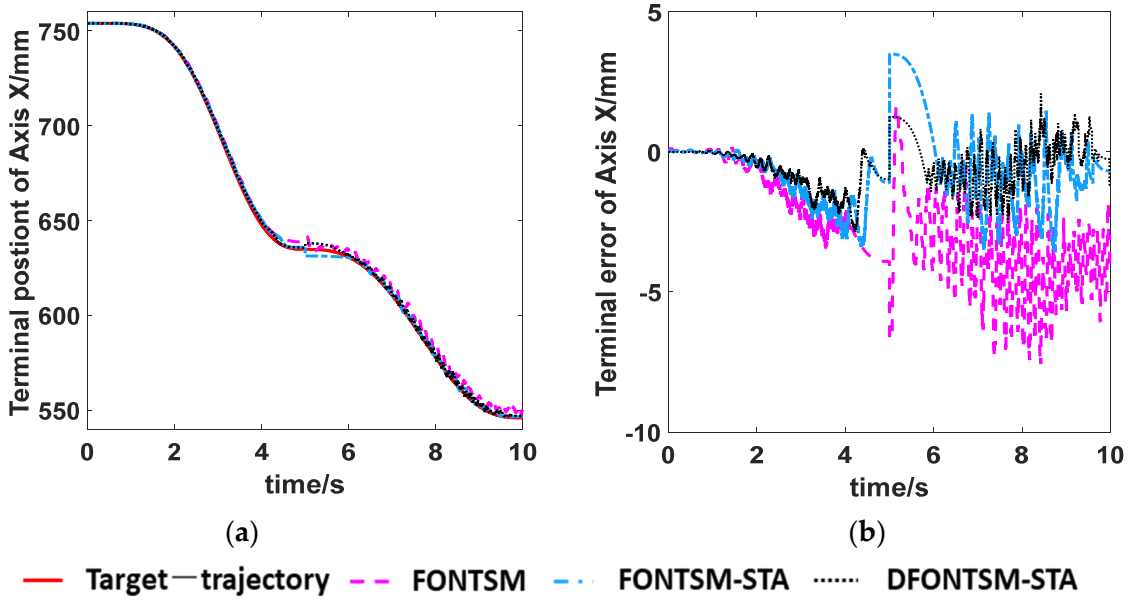

Figure 15. Terminal trajectory and its tracking error. (**a**): terminal trajectory on the X axis; (**b**): terminal tracking error on the X axis.

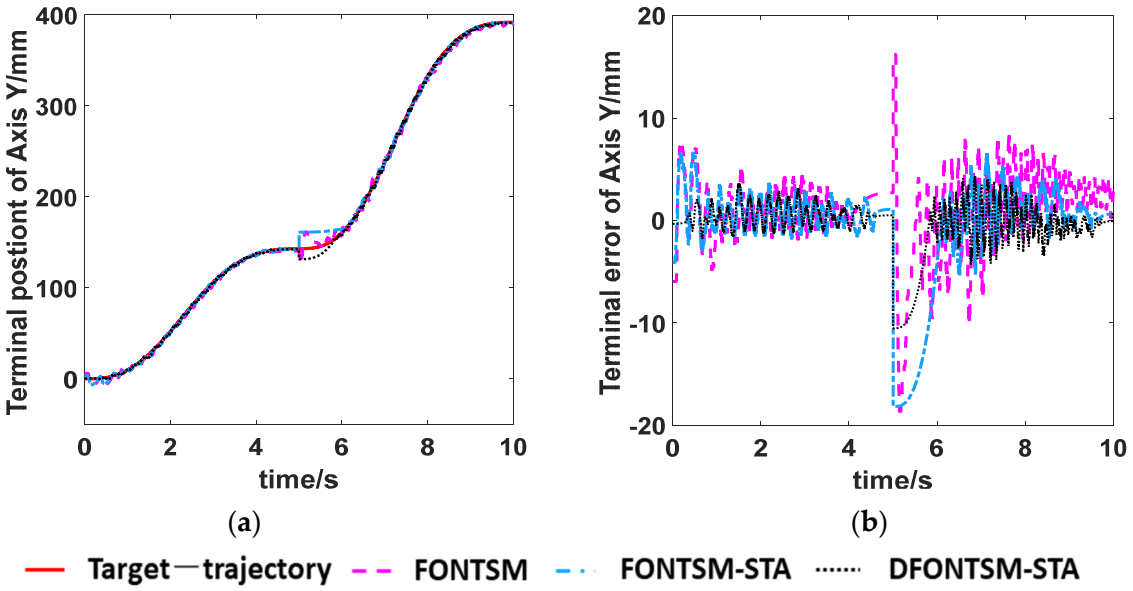

Figure 16. Terminal trajectory and its tracking error. (**a**): terminal trajectory on the Y axis; (**b**): terminal tracking error on the Y axis.

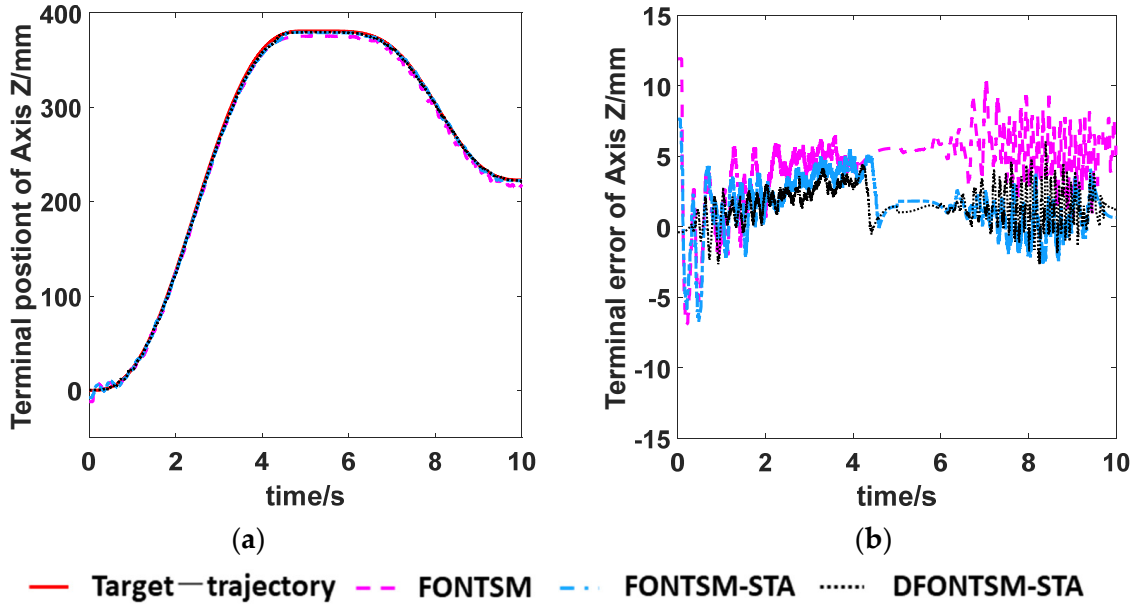

Figure 17. Terminal trajectory and its tracking error. (**a**): terminal trajectory on the Z axis; (**b**): terminal tracking error on the Z axis.

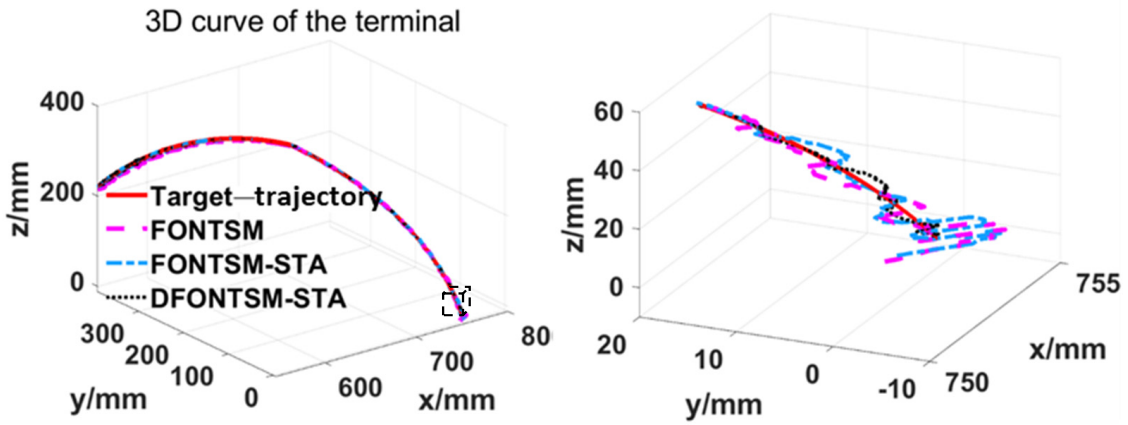

(**a**) (**b**)

Figure 18. Terminal motion under base coordination system. (**a**): Terminal trajectory tracking curve; (**b**): initial part of the terminal trajectory tracking curve.

6.3. Experiment Analysis

The convergence time is calculated when the absolute value of the tracking error is within the 1° (elbow joints) or 0.5° (shoulder joints), which is shown in Table 12.

Table 12. Convergence time for each joint.

$\|e\| \leq 0.5°$ or $\|e\| \leq 1°$	DFONTSM-STA (t_{conv})s	FONTSM-STA (t_{conv})s	FONTSM (t_{conv})s
Joint one	0	0.474	0.548
Joint two	0	0.075	0.229
Joint three	6.188	6.395	7.101
Joint four	5.562	5.934	7.057

Figures 10 and 12 are the angular tracking error of the three methods, which show the robustness of the FOSM control. Through experimental data, DFONTSM-STA control is superior in accurate and smooth position tracking performance. Compared with the FONTSM control and FONTSM-STA control, the error convergence time of joint one under DFONTSM-STA control is reduced by 0.548 s and 0.474 s respectively, and the error convergence time of joint two is reduced by 0.229 s and 0.075 s respectively. The error convergence speed of joint three under DFONTSM-STA control is speeded up by 43.5% and 33.6% respectively, and the error convergence speed of joint four is speeded up by 72.7% and 54.6% respectively. The DFONTSM-STA control can significantly improve the error convergence by dynamically changing the spatial position of the sliding mode manifold.

Figures 13 and 14 show the control torques required to drive the low-cost humanoid manipulator. Table 13 shows the maximum variation of the control torque chattering, which can reveal the chattering suppression effects of the three controllers in real-time position control. From Table 13, it can be concluded that the chattering of joints one to four under the FONTSM-STA control is suppressed by 47.8%, 9.6%, 52.2%, and 34.5% respectively compared with the FONTSM control, and the chattering of joints one to four under the DFONTSM-STA control is suppressed by 54.1%, 51.1%, 46.2%, and 55.1% respectively, with the comparison of the FONTSM control. Thus, the chattering suppression performance of DFONTSM-STA control is ahead of the other two control methods.

Table 13. The maximum variation of control torque in a small interval.

$\|\tau\|_{max}$ (t_p = 20 ms)	DFONTSM-STA	FONTSM-STA	FONTSM
Joint one	0.0095	0.0108	0.0207
Joint two	0.0112	0.0207	0.0229
Joint three	0.0204	0.0181	0.0379
Joint four	0.0151	0.022	0.0336

Figures 15–18 show the terminal motion performances of the low-cost humanoid manipulator. According to Figure 18, the DFONTSM-STA control can make the terminal faster and more accurate to tracking the target trajectory. The terminal tracking process of DFONTSM-STA control is smoother than FONTSM-STA control and FONTSM control, which can be illustrated by the terminal tracking trajectory that is decomposed to the X, Y, and Z direction of the base coordination. Compared with the FONTSM control, the motion accuracy of joints one to four of the DFONTSM-STA control embodied by the root mean square of joint tracking error is improved by 55.4% 51.1% 38.5%, and 32.8% respectively. Compared with the FONTSM-STA control, the motion accuracy of joints one to four is improved by 32.1%, 35.4%, 2.9%, and 42.6% respectively.

Table 14 shows the terminal root mean square error of the low-cost humanoid manipulator (S_{rmste}). The S_{rmste} of FOTNSM-STA control and FONTSM control between the terminal and the target trajectory surpasses 5 mm, which indicates the tracking performances of the anthropomorphic trajectory are not quite well. Compared with FONTSM-STA control, the S_{rmste} on the X, Y, and Z coordinate axes of the base coordination under DFONTSM-TSM control is reduced by 35.5%, 45.4%, and 20.9%, respectively. Compared with FONTSM-STA control, the S_{rmste} on the X, Y, and Z coordinate axes of the base coordination under DFONTSM-TSM control is reduced by 69.4%, 36.8%, and 61.2%, respectively. The S_{rmste} of DFOTNSM-TSM control between the terminal and the target trajectory is limited to 3 mm and reduced by 23.7% and 53.3% compared with FONTSM-STA and FONTSM control.

Table 14. Terminal root mean square error of the humanoid manipulator.

S_{rmste} (mm)	DFONTSM-STA	FONTSM-STA	FONTSM
Axis x	0.983	1.524	3.212
Axis y	2.584	4.730	4.090
Axis z	1.984	2.509	5.111
Distance between the terminal and the target	3.403	5.567	7.292

To sum up, the experiments confirm that The DFONTSM-STA control, compared with FONTSM-STA control and FONTSM control, can further improve the accuracy and smoothness of the terminal tracking performances and basically realize anthropomorphic motion of the low-cost humanoid manipulator.

7. Conclusions

A DFONTSM-STA control was proposed for a low-cost humanoid manipulator by combining the dynamic fractional-order nonsingular terminal sliding mode manifold with the super-twisting reaching law. Experiments were conducted to control the low-cost humanoid manipulator and showed that the proposed control method can effectively improve error convergence speed, tracking accuracy, and chattering suppression ability. In error convergence speed, the errors of joints one and two were converged at the beginning while joint three was speeded up by 43.5% and 33.6%, and joint four was speeded up by 72.7% and 54.6% compared with FONTSM and FONTSM-STA controllers. In chattering suppressing, suppression performances of joints, one to four were enhanced by 54.1%, 51.1%, 46.2%, and 55.1%, respectively, compared with FONTSM control. In trajectory tracking performance, compared with FONTSM control and FONTSM-STA control, the tracking accuracy of DFONTSM-STA control was promoted by 53.3% and 23.7% respectively. Simulation and

experimental results illustrate the superiority of the proposed DFONTSM-STA control for the low-cost humanoid manipulator.

The proposed DFONTSM-STA controller is applicable to humanoid manipulators that require fast error convergence and accurate trajectory tracking movements. The dynamic model of the low-cost humanoid manipulator is complex, and there exists the problem of big calculations in solving control inputs. Therefore, the adaptive fuzzy method will be studied to estimate model uncertainties and disturbances in future research work.

Author Contributions: Conceptualization, H.D.; Data curation, R.H., X.X. and Y.Z.; Funding acquisition, Y.Z. and H.D.; Methodology, R.H.; Project administration, X.X., Y.Z. and H.D.; Software, R.H. and X.X.; Supervision, H.D.; Validation, R.H., X.X. and Y.Z.; Writing—original draft, R.H.; Writing—review & editing, R.H. and H.D. All authors have read and agreed to the published version of the manuscript.

Funding: This research was funded in part by the National Key Research and Development Program of China under grant number 2018YFB1307203, in part by National Natural Science Foundation of China under Grant 52275297, and in part by the Project of State Key Laboratory of High Performance Complex Manufacturing, Central South University under Grant ZZYJKT2021-17.

Data Availability Statement: Not applicable.

Conflicts of Interest: The authors declare no conflict of interest.

Abbreviations

The following abbreviations are used in this manuscript:

Acronyms	Definition
D-H	Denavit-Hartenberg
PC	Personal computer
3D	Three dimensional
RL	Riemann-Liouville
EtherCAT	Ethernet control automation technology
CANopen	Controller area network open
FO	Fractional-order
FOSM	Fractional-order sliding mode
FONTSM	Fractional-order nonsingular terminal sliding mode
DFONTSM	Dynamic fractional-order nonsingular terminal sliding mode
STA	Super-twisting algorithm
STSM	Super-twisting sliding mode
FONTSM-STA	Fractional- order nonsingular terminal super-twisting sliding mode
DFONTSM-STA	Dynamic fractional- order nonsingular terminal super-twisting sliding mode

References

1. Kaneko, K.; Kaminaga, H.; Sakaguchi, T.; Kajita, S.; Morisawa, M.; Kumagai, I.; Kanehiro, F. Humanoid robot HRP-5P: An electrically actuated humanoid robot with high-power and wide-range joints. *IEEE Robot. Autom. Lett.* **2019**, *4*, 1431–1438. [CrossRef]
2. Zhang, B.; Xiong, R.; Wu, J. Kinematics and trajectory planning of a novel humanoid manipulator for table tennis. In Proceedings of the 2011 International Conference on Electrical and Control Engineering, Yichang, China, 16–18 September 2011; pp. 3047–3051. [CrossRef]
3. Khusainov, R.; Klimchik, A.; Magid, E. Humanoid robot kinematic calibration using industrial manipulator. In Proceedings of the 2017 International Conference on Mechanical, System and Control Engineering (ICMSC), St. Petersburg, Russia, 19–21 May 2017; pp. 184–189.
4. Sarajchi, M.; Al-Hares, M.K.; Sirlantzis, K. Wearable Lower-Limb Exoskeleton for Children With Cerebral Palsy: A Systematic Review of Mechanical Design, Actuation Type, Control Strategy, and Clinical Evaluation. *IEEE Trans. Neural Syst. Rehabil. Eng.* **2021**, *29*, 2695–2720. [CrossRef] [PubMed]
5. Rehman, I.U.; Javed, S.B.; Chaudhry, A.M.; Azam, M.R.; Uppal, A.A. Model-based dynamic sliding mode control and adaptive Kalman filter design for boiler-turbine energy conversion system. *J. Process Control* **2022**, *116*, 221–233. [CrossRef]
6. Mechali, O.; Xu, L.M.; Xie, X.M.; Iqbal, J. Theory and practice for autonomous formation flight of quadrotors via distributed robust sliding mode control protocol with fixed-time stability guarantee. *Control Eng. Pract.* **2022**, *123*, 105150. [CrossRef]

7. Bano, S.; Azam, M.R.; Uppal, A.A.; Javed, S.B.; Bhatti, A.I. Robust p53 recovery using chattering free sliding mode control and a gain-scheduled modified Utkin observer. *J. Theor. Biol.* **2021**, *532*, 110914. [CrossRef]
8. Qin, L.; Liang, L.; Liu, F.; Jin, Z. The application of adaptive backstepping sliding mode for hybrid humanoid robot arm trajectory tracking control. In Proceedings of the 2013 International Conference on Advanced Mechatronic Systems, Luoyang, China, 25–27 September 2013; pp. 730–735.
9. Kuan, J.Y.; Huang, H.P. Independent joint dynamic sliding mode control of a humanoid robot arm. In Proceedings of the 2008 IEEE International Conference on Robotics and Biomimetics, Dali, China, 6–8 December 2019; pp. 602–607.
10. Sanchez-Magos, M.; Ballesteros-Escamilla, M.; Cruz-Ortiz, D.; Salgado, I.; Chairez, I. Terminal sliding mode control of a virtual humanoid robot. In Proceedings of the 2019 6th International Conference on Control, Decision and Information Technologies (CoDIT), Paris, France, 23–26 April 2019; pp. 726–731.
11. Ganjefar, S.; Sarajchi, M.H.; Hoseini, S.M.; Shao, Z. Lambert W Function Controller Design for Teleoperation Systems. *Int. J. Precis. Eng. Manuf.* **2019**, *20*, 101–110. [CrossRef]
12. Gao, W.; Hung, J.C. Variable structure control of nonlinear systems: A new approach. *IEEE Trans. Ind. Electron.* **1993**, *40*, 45–55.
13. Ullah, M.I.; Ajwad, S.A.; Irfan, M.; Iqbal, J. Non-linear Control Law for Articulated Serial Manipulators: Simulation Augmented with Hardware Implementation. *Elektron. Elektrotechnika* **2016**, *22*, 3–7. [CrossRef]
14. Utkin, V. Variable structure systems with sliding modes. *IEEE Trans. Autom. Control* **1977**, *22*, 212–220. [CrossRef]
15. Fuh, C.C. Variable-thickness boundary layers for sliding mode control. *J. Mar. Sci. Technol.* **2008**, *16*, 7. [CrossRef]
16. Young, K.D.; Utkin, V.; Ozguner, U.A. control engineer's guide to sliding mode control. *IEEE Trans. Control Syst. Technol.* **1999**, *7*, 328–342. [CrossRef]
17. Soheil, G.; Mohammad, H.S.; Mahmoud Hoseini, S. Teleoperation Systems Design Using Singular Perturbation Method and Sliding Mode Controllers. *J. Dyn. Syst. Meas. Control* **2014**, *136*, 051005.
18. Chen, Y.-Q.; Wei, Y.-H.; Wang, Y. On 2 types of robust reaching laws. *Int. J. Robust Nonlinear Control* **2018**, *28*, 2651–2667. [CrossRef]
19. Giap, V.-N.; Huang, S.-C. Effectiveness of fuzzy sliding mode control boundary layer based on uncertainty and disturbance compensator on suspension active magnetic bearing system. *Meas. Control* **2020**, *53*, 934–942. [CrossRef]
20. Tayebi-Haghighi, S.; Piltan, F.; Kim, J.M. Robust Composite High-Order Super-Twisting Sliding Mode Control of Robot Manipulators. *Robotics* **2018**, *6*, 13. [CrossRef]
21. Floquet, T.; Barbot, J.P.; Perruquetti, W. Higher order sliding mode stabilization for a class of non holomic perturbed system. *Automatica* **2003**, *39*, 1077–1083. [CrossRef]
22. Davila, J.; Fridman, L.; Levant, A. Second-order sliding-mode observer for mechanical systems. *IEEE Trans. Autom. Control* **2005**, *50*, 1785–1789. [CrossRef]
23. Davila, J.; Fridman, L.; Poznyak, A. Observation and identification of mechanical systems via second order sliding modes. In *International Workshop on Variable Structure Systems*; IEEE: New York, NY, USA, 2006; pp. 232–237.
24. Guzmán, E.; Moreno, J.A. Super-twisting observer for second-order systems with time-varying coefficient. *IET Control Theory Appl.* **2015**, *9*, 553–562. [CrossRef]
25. Mu, C.; Sun, C. A new finite time convergence condition for super-twisting observer based on Lyapunov analysis. *Asian J. Control* **2015**, *17*, 1050–1060. [CrossRef]
26. Tenoch, G.; Jaime, A.M.; Fridman, L. Variable Gain Super-Twisting Sliding Mode Control. *IEEE Trans. Autom. Control* **2012**, *57*, 2100–2105.
27. Utkin, V. On convergence time and disturbance rejection of super-twisting control. *IEEE Trans. Autom. Control* **2013**, *58*, 2013–2017. [CrossRef]
28. Lochan, K.; Singh, J.P.; Roy, B.K. Adaptive time-varying super-twisting global SMC for projective synchronisation of flexible manipulator. *Nonlinear Dyn.* **2018**, *93*, 2071–2088. [CrossRef]
29. Nasim, U.; Yasir, M.; Jawad, A.; Amjad, A.; Jamshed, I. UAVS-UGV Leader Follower Formation Using Adaptive Non-Singular Terminal Super Twisting Sliding Mode Control. *IEEE Access* **2021**, *5*, 3081483.
30. Moreno, J.A.; Osorio, M. A Lyapunov approach to second-order sliding mode controllers and observers. In Proceedings of the 47th IEEE Conference on Decision and Control, Cancún, Mexico, 9–11 December 2008; pp. 2856–2861.
31. Kali, Y.; Saad, M.; Benjelloun, K.; Khairallah, C. Super-twisting algorithm with time delay estimation for uncertain robot manipulators. *Nonlinear Dyn.* **2018**, *93*, 557–569. [CrossRef]
32. Yin, C.; Chen, Y.; Zhong, S.-M. Fractional-order sliding mode based extremum seeking control of a class of nonlinear systems. *Automatica* **2014**, *50*, 3173–3181. [CrossRef]
33. Chen, D.; Zhang, J.D.; Li, Z.K. A Novel Fixed-Time Trajectory Tracking Strategy of Unmanned Surface Vessel Based on the Fractional Sliding Mode Control Method. *Electronics* **2022**, *11*, 726. [CrossRef]
34. Maaruf, M.; Khalid, M. Global sliding-mode control with fractional-order terms for the robust optimal operation of a hybrid renewable microgrid with battery energy storage. *Electronics* **2021**, *11*, 88. [CrossRef]
35. Zhu, L.K.; Chen, X.R.; Qi, X.; Zhang, J. Research on Fractional-Order Global Fast Terminal Sliding Mode Control of MDF Continuous Hot-Pressing Position Servo System Based on Adaptive RBF Neural Network. *Electronics* **2022**, *11*, 1117. [CrossRef]
36. Aghababa, M.P. A fractional-order controller for vibration suppression of uncertain structures. *ISA Trans.* **2013**, *52*, 881–887. [CrossRef]

37. Cuong, H.M.; Dong, H.Q.; Trieu, P.V.; Tuan, L.A. Adaptive fractional-order terminal sliding mode control of rubber-tired gantry cranes with uncertainties and unknown disturbances. *Mech. Syst. Signal Proc.* **2021**, *154*, 107601. [CrossRef]
38. Wang, Y.; Yan, F.; Zhu, K.; Chen, B.; Wu, H. A new practical robust control of cable-driven manipulators using time-delay estimation. *Int. J. Robust Nonlinear Control.* **2019**, *29*, 3405–3425. [CrossRef]
39. Duc, T.M.; Hoa, N.V.; Dao, T.P. Adaptive Fuzzy Fractional-Order Nonsingular Terminal Sliding Mode Control for a Class of Second-Order Nonlinear Systems. *J. Comput. Nonlinear Dyn.* **2018**, *13*, 031004. [CrossRef]
40. Tuan, L.A. Neural observer and adaptive fractional-order backstepping fast-terminal sliding-mode control of RTG cranes. *IEEE Trans. Ind. Electron.* **2021**, *68*, 434–442. [CrossRef]
41. Nojavanzadeh, D.; Badamchizadeh, M. Adaptive Fractional-order Non-singular Fast Terminal Sliding Mode Control for Robot Manipulators. *IET Control Theory Appl.* **2016**, *10*, 1565–1572. [CrossRef]
42. Su, L.; Guo, X.; Ji, Y.; Tian, Y. Tracking control of cable-driven manipulator with adaptive fractional-order nonsingular fast terminal sliding mode control. *J. Vib. Control* **2021**, *27*, 2482–2493. [CrossRef]
43. Wang, Y.Y.; Peng, J.W.; Zhu, K.W.; Chen, B.; Wu, H.T. Adaptive PID-fractional-order nonsingular terminal sliding mode control for cable-driven manipulators using time-delay estimation. *Int. J. Syst. Sci.* **2020**, *51*, 3118–3133. [CrossRef]
44. Wang, Y.Y.; Gu, L.Y.; Xu, Y.H.; Cao, X.X. Practical tracking control of robot manipulators with continuous fractional-order nonsingular terminal sliding mode. *IEEE Trans. Ind. Electron.* **2016**, *63*, 6194–6204. [CrossRef]
45. Wang, Y.Y.; Chen, J.W.; Yan, F.; Zhu, K.W.; Chen, B.; Wang, Y. Adaptive super-twisting fractional-order nonsingular terminal sliding mode control of cable-driven manipulators. *ISA Trans.* **2018**, *75*, 163–180. [CrossRef]
46. Zhang, Y.Y.; Yang, X.H.; Wei, P.; Liu, P.X. Fractional-order adaptive non-singular fast terminal sliding mode control with time delay estimation for robotic manipulators. *IET Control Theory Appl.* **2020**, *14*, 2556–2565. [CrossRef]
47. Hu, R.; Deng, H.; Zhang, Y. Novel dynamic-sliding-mode-manifold-based continuous fractional-order nonsingular terminal sliding mode control for a class of second-order nonlinear systems. *IEEE Access* **2020**, *8*, 19820–19829. [CrossRef]
48. Kilbas, A.; Srivastava, H.M.; Trujillo, J.J. Fractional integrals and fractional derivatives. In *Theory Applications of Fractional Differential Equations*; Elsevier: Amsterdam, The Netherlands, 2006; pp. 69–133.